Drop Size Distributions Measured by a 2D Video Disdrometer: Comparison with Dual-Polarization Radar Data

TERRY J. SCHUUR AND ALEXANDER V. RYZHKOV

Cooperative Institute for Mesoscale Meteorological Studies, University of Oklahoma, Norman, Oklahoma

DUSAN S. ZRNIĆ

National Severe Storms Laboratory, Norman, Oklahoma

MICHAEL SCHÖNHUBER

Joanneum Research, Graz, Austria

(Manuscript received 14 February 2000, in final form 22 August 2000)

ABSTRACT

An analysis of drop size distributions (DSDs) measured in four very different precipitation regimes is presented and is compared with polarimetric radar measurements. The DSDs are measured by a 2D video disdrometer, which is designed to measure drop size, shape, and fall speed with unprecedented accuracy. The observations indicate that significant DSD variability exists not only from one event to the next, but also *within* each system. Also, despite having vastly different storm structures and maximum rain rates, large raindrops with diameters greater than 5 mm occurred with each system. By comparing the occurrence of large drops with rainfall intensity, the authors find that the largest median diameters are not always associated with the heaviest rainfall, but are sometimes located either in advance of convective cores or, occasionally, in stratiform regions where rainfall rates are relatively low. Disdrometer and polarimetric radar measurements of radar reflectivity Z, differential reflectivity Z_{DR}, specific differential phase K_{DP}, and $R(Z)$ and $R(K_{DP})$ rain-rate estimators are compared in detail. Overall agreement is good, but it is found that both $R(Z)$ and $R(K_{DP})$ underestimate rain rate when the DSD is dominated by small drops and overestimate rain rate when the DSD is dominated by large drops. The results indicate that a classification of different rain types (associated with different DSDs) should be an essential part of polarimetric rainfall estimation. Furthermore, observations suggest that Z_{DR} is a key parameter for making such a distinction. Last, the authors compute and compare maximum and average of gamma shape, slope, and intercept parameters for all four precipitation events. Potential measurement errors with the 2D video disdrometer are also discussed.

1. Introduction

Natural variations in drop size distributions (DSDs) substantially limit the accuracy of radar-derived rainfall estimates. Though less susceptible than conventional radar methods, even polarimetric methods of rainfall estimation are known to depend on variability in raindrop spectra. For example, DSDs with an anomalously large number of small (large) raindrops will commonly result in an underestimation (overestimation) of rainfall (Ryzhkov et al. 1999). These known dependencies underscore a need to better understand natural DSD variations in precipitation events. Indeed, observations indicate that significant DSD variability exists not only from one event to the next, but even within individual precipitation events (e.g., Waldvogel 1974; Tokay and Short 1996; Atlas et al. 1999).

Over the years, numerous attempts have been made to investigate raindrop spectra variability, develop mathematical functional fits to typical spectra and, subsequently, to formulate radar-based rainfall relationships. In a study that examined all 69 Z–R relationships listed in Battan (1973), Ulbrich (1983) derived a range for typical shape (μ), slope (Λ), and intercept (N_0) parameters associated with a gamma function fit. The gamma function is represented by

$$N(D) = N_0 D^{\mu} \exp(-\Lambda D), \tag{1}$$

where D is the drop equivalent diameter and Λ is related to the median volume diameter D_0 by the relationship,

$$\Lambda D_0 = 3.67 + \mu. \tag{2}$$

Ulbrich found that typical values for μ, D_0, and N_0 in naturally occurring raindrop spectra are $-1 < \mu < 4$,

Corresponding author address: Dr. Terry J. Schuur, National Severe Storms Laboratory, 1313 Halley Circle, Norman, OK 73069.
E-mail: terry.schuur@nssl.noaa.gov

$0.5 < D_0 < 2.5$, and $10^{3.2-\mu} \exp(2.8\mu) < N_0 < 10^{4.5-\mu} \exp(3.57\mu)$. Those values, in turn, have been used to develop and to evaluate new polarimetric radar rainfall estimators (e.g., Chandrasekar et al. 1990; Scarchilli et al. 1993; Ryzhkov and Zrnić 1995).

Most experimental measurements of DSDs in different geographical areas have been performed with impact disdrometers such as the Joss–Waldvogel disdrometer (Joss and Waldvogel 1967) and an Applied Physics Laboratory, Johns Hopkins University, disdrometer (Rowland 1976). Recently, a new kind of instrument with superior characteristics, a 2D video disdrometer, was designed by the Joanneum Research Company of Graz, Austria (Schönhuber et al. 1997). Simultaneous DSD observations with impact and video disdrometers made by Tokay et al. (1999) and Williams et al. (2000) indicate that impact-type disdrometers seriously undersample very big raindrops ($D > 5.4$ mm) and very small raindrops ($D < 1.5$ mm). As was shown by Schuur et al. (1999), large raindrops with D greater than 5 mm may be common, at least in the U.S. Great Plains, where many drops originate from melting hail aloft and may contain ice cores inside. This result is significant because many radar measurands (particularly Z and differential reflectivity Z_{DR}) are heavily weighted toward larger drop sizes.

Surprisingly, DSD variability in the Great Plains region, where a very broad range of rain types occurs, is not well documented in the literature. This fact and the availability of the 2D video disdrometer at the National Severe Storms Laboratory (NSSL) prompted us to start systematic measurements of DSDs in central Oklahoma and to use them for interpretation of simultaneous dual-polarization radar data and for assessment of different rainfall estimators. In this paper, we perform joint analyses of high-resolution 2D video disdrometer data and polarimetric radar measurands and compare rainfall estimates from the disdrometer and the radar rainfall-rate estimators. We focus on examining DSD variability within four distinctly different precipitation events: 1) relatively weak convective rainbands, 2) a long-lived, synoptic-scale system that consisted of widespread stratiform precipitation and embedded strong convection, 3) an intense leading-line/trailing-stratiform mesoscale convective system, and 4) a supercell thunderstorm that contained approximately 2-cm hail. In section 2, we discuss the 2D video disdrometer and the methods by which the disdrometer and radar data were analyzed. In section 3, we present a comparison of the disdrometer and polarimetric radar data for the above four precipitation events. In section 4, we compare the parameters resulting from gamma functional fits to the DSDs of the four case studies. A short discussion of potential disdrometer catchment and measurement errors is presented in section 5. In section 6, we summarize the conclusions of this study. In the appendix, we present a statistical analysis that addresses the difficulties that arise when attempting to compare disdrometer measurements with those of the much larger radar resolution volume.

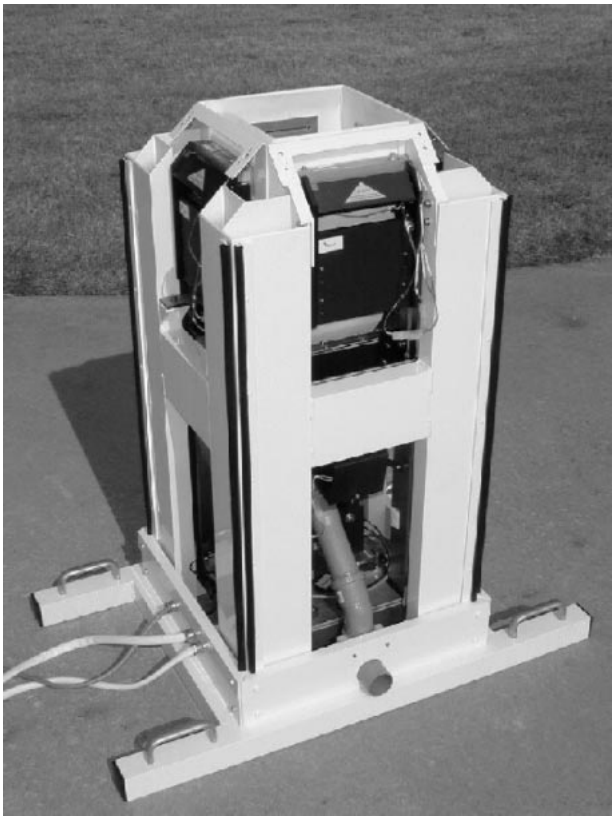

FIG. 1. Picture of the NSSL 2D video disdrometer sensor unit (SU) with cover and two side panels removed. Picture is taken from the corner of the A and B lamp sides of the SU. Lamps are located immediately below the white cross bar, and mirrors that redirect light source through slit plates are located behind the inclined surface of the cover (which has been removed for this picture). One of the four slit plates is visible just below the orifice on the opposite side of the SU. Line scan cameras are not visible in this picture but are located on the panel that can be seen at the base of the instrument.

2. Data analysis

a. Disdrometer measurements

The DSDs used in this study were measured by a 2D video disdrometer developed by Joanneum Research (e.g., Schönhuber et al. 1997). The disdrometer consists of three interdependent units: 1) a sensor unit (SU), which samples the data, 2) an outdoor electronics unit (OEU), which monitors the operation of the SU and stores the initial data packets, and 3) an indoor user terminal (IUT), which receives data from the OEU, processes the image data to determine drop size, shape, and fall speed, and displays the information in real time. A picture of the SU with two of its side panels removed is shown in Fig. 1. The instrument is approximately 1 m high and has a 25 cm × 25 cm orifice at the top (though the actual measurement area is a somewhat smaller nested area,

discussed below). Just below the orifice, an inclined surface slopes outward toward the side of the SU, which, at its maximum width, has a rectangular dimension of 50 cm × 50 cm. A velcro fabric that is designed to prevent splashing drops from entering the measurement area covers the inclined surface. The SU is fully self-contained, is water tight, and has sides that are easily removed in order that lamps may be replaced or calibration work performed. A small hole at the base of the opening is connected to a pipe that funnels rain water through the SU and out onto the ground.

The disdrometer is designed to obtain two (hereinafter referred to as A and B) orthogonal side images of each raindrop. Two lamps that are nested within the sensor unit provide light sources that are first redirected by mirrors and then passed through slit plates that are located on the sides of the orifice. This creates A (upper) and B (lower) planes of light that transect the approximate 10 cm × 10 cm measurement area with a vertical separation of ~6.2 mm. Additional slit plates and mirrors located on the opposite side of the orifice then redirect the planes downward onto two line scan cameras that are located near the base of the instrument. The line scan cameras sample each plane at a rate of ~29 μs and a horizontal resolution of ~200 μm. Therefore, as a raindrop falls through the measurement area, several line scans of each image are recorded from two sides and two different heights. The line scan data from each camera are then instantaneously transmitted by cable to the OEU where they are packaged into 3-s files and transmitted by a radio frequency link (in our setup) to the IUT, which is located in an office approximately 100 m from the disdrometer site. The IUT software matches the A and B images, determines drop shape, size, oblateness, and fall speed for each drop, and displays all of the above (along with a rain rate and DSD) in real time.

This measurement principle, which is similar in design to that used by aircraft optical array probes (e.g., Knollenberg 1970), allows the disdrometer to measure drop size, shape, and fall speed (because of the vertical separation in the A and B planes) with unprecedented accuracy. In particular, drops with D less than 1.5 mm [typically underrepresented in impact-type disdrometer measurements, e.g., Tokay et al. (1999)], and greater than 5 mm [not resolved by impact-type disdrometer measurements, e.g., Rowland (1976)], are both accurately measured by the 2D video disdrometer. This fact leads to more meaningful functional fits to observed DSDs and more accurate comparisons with polarimetric radar measurements. For all cases presented in this study, the disdrometer was located ~41.5 km SE [(X, Y) = (31.8 km, −26.6 km)] of the NSSL Cimarron polarimetric radar (hereinafter referred to as CIM) and ~20.4 km SW [(X, Y) = (−17.3 km, −10.8 km)] of the National Weather Service Weather Surveillance Radar, 1988 Doppler (WSR-88D) operational radar (hereinafter referred to as KTLX).

After collection, the disdrometer data were processed to produce 1-min-averaged DSDs. Using the method of moments (Ulbrich and Atlas 1998), gamma functions were then fit to all 1-min-averaged DSDs wherein the number of drops exceeded 25 and the rain rate exceeded 0.5 mm h^{-1}. These thresholds were chosen to ensure that a sufficient number of drops were present to obtain a meaningful functional fit to the data. To account better for occasional low concentrations of large drops, which are important contributors to polarimetric measurements, 5-min-averaged DSDs were also computed and are occasionally presented in this paper. Furthermore, because the gamma μ and N_0 parameters are known to be correlated (Ulbrich 1983), we also investigate DSDs that have been normalized with respect to liquid water content (Dou et al. 1999; Testud et al. 2000). The normalized gamma distribution parameters of N_0^*, D_0, and μ that result from this process have the additional advantage that 1) the three variables are independent measures of the absolute concentration of drops, the medium volume diameter, and the spectrum shape, 2) N_0^* is equal to N_0 of the exponential distribution when μ is equals to 0, and 3) the liquid water content is independent of μ.

Once the gamma μ, Λ, and N_0 parameters are obtained using the method of moments, other distribution shape parameters can be computed using the procedures presented in Ulbrich (1983). In this paper, we primarily present and discuss D_0 in relation to the measured polarimetric measurands because it is a good indicator of the drop size that dominates the DSD, can often be related to the microphysical processes within the cloud, and is probably one of the better DSD parameters to derive from the measurement of Z_{DR} (Seliga et al. 1986). However, because D_0 computed from Eq. (2) is only valid for infinite spectra (e.g., Ulbrich 1983; 1985; Ulbrich and Atlas 1998), we also calculate D_0 using the more appropriate formulation (for finite spectra) of

$$2\int_{D_{\min}}^{D_0} D^3 N(D)\, dD = \int_{D_{\min}}^{D_{\max}} D^3 N(D)\, dD. \qquad (3)$$

In this paper, D_0s computed using this method (using a minimum threshold of 50 drops) are presented in the case studies section because they provide the most accurate representation of the true median volume diameter associated with the DSD. For comparison, a summary of D_0s computed from the theoretical functional fit is presented in section 4.

For a more direct comparison to the polarimetric radar measurements, the DSDs were also used to compute (see the appendix) radar reflectivity Z, differential reflectivity Z_{DR}, and specific differential phase K_{DP}. Although the 2D video disdrometer is designed to obtain high-resolution measurements of drop shape, airflow around the disdrometer during high-wind events occasionally resulted in disturbances that distorted the shapes of measured drops (discussed in more detail in section 4). Therefore, the disdrometer Z_{DR}s and K_{DP}s presented here

were computed using the equilibrium aspect ratio presented by Beard and Chuang (1987). That is,

$$a/b = 1.0048 - 0.0057D - 2.628D^2 + 3.682D^3 - 1.677D^4, \quad (4)$$

where D (cm) is the equivalent diameter as measured by the disdrometer.

b. Radar measurements

During disdrometer data collection, CIM recorded Z, Z_{DR}, and K_{DP}, while KTLX recorded Z. We use the data collected by both radars at the elevation angle of 0.5°, for which the center of the radar beam over the disdrometer was about 350 and 175 m for CIM and KTLX, respectively. KTLX data were updated every 5 min. The update time for CIM varied between 1 and 3 min.

The estimate of K_{DP} is obtained as a slope of a least squares linear fit of the total differential phase Φ_{DP} along a radial. The accuracy of the K_{DP} estimate depends on the range-averaging interval. As recommended for CIM by Ryzhkov and Zrnić (1996), averaging in range for this case was performed over 17 successive gates if Z was greater than or equal to 40 dBZ (corresponding approximately to $R > 10$ mm h^{-1}), and over 49 gates if Z was less than 40 dBZ. Hence, depending on gate spacing, which varies between 0.15 and 0.24 km, the effective radial resolution of the K_{DP} estimate is between 2.5 and 3.8 km for moderate and heavy rain and between 7.3 and 11.4 km for light precipitation. No radial averaging was performed for the radar reflectivity data. A running-average window containing 9 successive gates was used to smooth differential reflectivity data.

To compare radar and disdrometer point measurements, we use CIM Z, Z_{DR}, and K_{DP} data at seven successive gates and two adjacent azimuths centered on the disdrometer location. As suggested by Ryzhkov and Zrnić (1996), Z and K_{DP} were converted into rain rates R at each of these 14 gates using the standard WSR-88D relation

$$Z = 300R^{1.4}, \quad (5)$$

to retrieve $R(Z)$ and the formula

$$R(K_{DP}) = 40.6|K_{DP}|^{0.866}\ \mathrm{sign}(K_{DP}) \quad (6)$$

to obtain the polarimetric estimate of rain rate. We compare mean values of $R(Z)$ and $R(K_{DP})$ (computed by averaging of the corresponding estimates at each of 14 gates) with the disdrometer rain rate and also $R(Z)$ and $R(K_{DP})$ rather than from simple averaging of Z and K_{DP} over 14 gates. The latter averaging, however, was used to estimate mean radar value of Z_{DR}.

Because of radar calibration problems on CIM, we compare time series of mean Z obtained from both CIM and KTLX for the disdrometer location during the entire rain event and correct the radar reflectivity from CIM by matching these two time series.

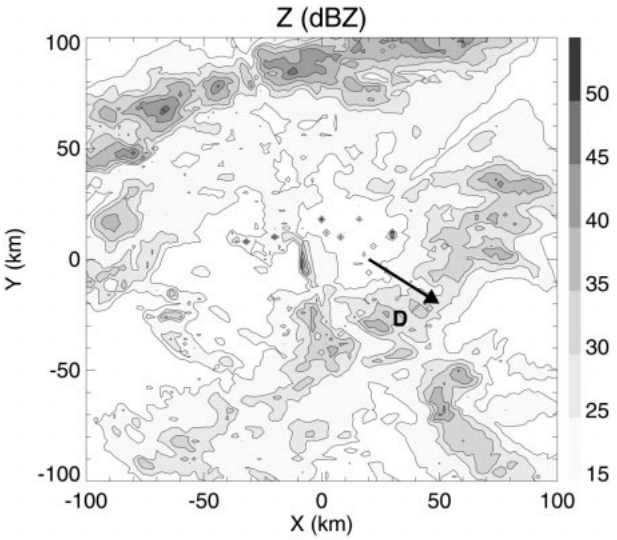

FIG. 2. Low-level radar reflectivity (dBZ) of the weak convective rainband event at 1943 UTC (0.2 h in Figs. 3 and 4). The NSSL Cimarron polarimetric radar (CIM) is located at the center of the figure at $(X, Y) = (0.0, 0.0)$. The disdrometer location is indicated by the bold "D" at $(X, Y) = (31.8, -26.6)$. Arrow depicts direction of storm motion. Figure has been constructed from 0.5° CIM base scan data.

3. Case studies

a. Weak convective rainbands

On 20 April 1998, a series of weak, early-afternoon convective showers that were organized into narrow rainbands passed through central Oklahoma. Disdrometer data collection started shortly after the beginning of this event. The disdrometer recorded 6.7 mm of rain over a continuous 2.8-h period; a rain gauge at an Oklahoma Mesonet site (located 3 km NW of the disdrometer) recorded 7.3 mm of rainfall. The maximum rain rate recorded by the disdrometer was 10.58 mm h^{-1}. Figure 2 depicts CIM low-level radar reflectivity at 1943 UTC (0.2 h in Figs. 3 and 4) and shows two rainbands with maximum radar reflectivities of 40 dBZ. Storm motion was toward the SE. Although the rainfall was continuous, regions between the rainbands often had radar reflectivities of less than 15 dBZ and occasional rain rates below 0.5 mm h^{-1}.

The DSD evolution for this event is shown in Fig. 3. It complements Fig. 4, which depicts a four-panel time series comparison of disdrometer and radar Z, Z_{DR}, K_{DP}, and rainfall rates. Figure 3 is constructed to display the concentrations at each size for the duration of the precipitation event. As can be seen in Fig. 3, three drops with D greater than 5 mm were observed during this event, all at times that were nearly coincident with the peak rainfall rate. However, large drops were also observed at much smaller rain rates. For example, between approximately 0.75 and 0.85 h, several drops with D greater than 4 mm occurred at a rainfall rate of only 3 mm h^{-1}. During this time interval, the largest D_0s of

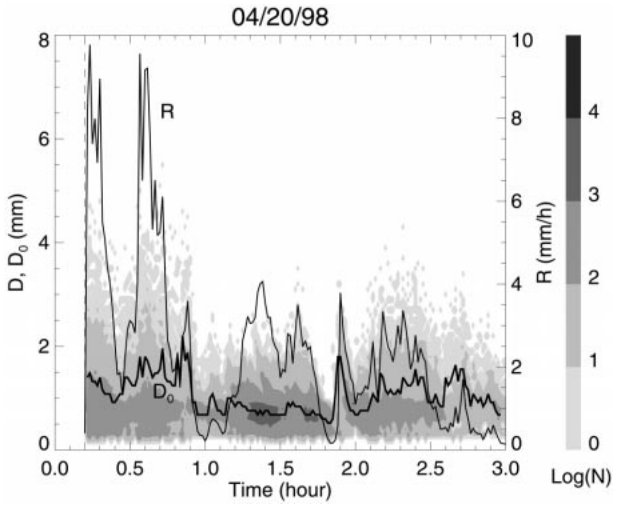

FIG. 3. Time series of 1-min-averaged DSD evolution and rain rate for the weak convective rainband event (20 Apr 1998). Concentrations for each drop size (D) are depicted by logarithmic shading contours, with the five intensity levels representing concentrations of $10^0 < N < 10^1$, $10^1 < N < 10^2$, $10^2 < N < 10^3$, $10^3 < N < 10^4$, and $10^4 < N < 10^5$, respectively. Light solid line represents corresponding disdrometer rain rate (mm h^{-1}); dark solid line represents corresponding median volume diameter (mm). Dashed vertical line depicts time of the low-level reflectivity plot in Fig. 2.

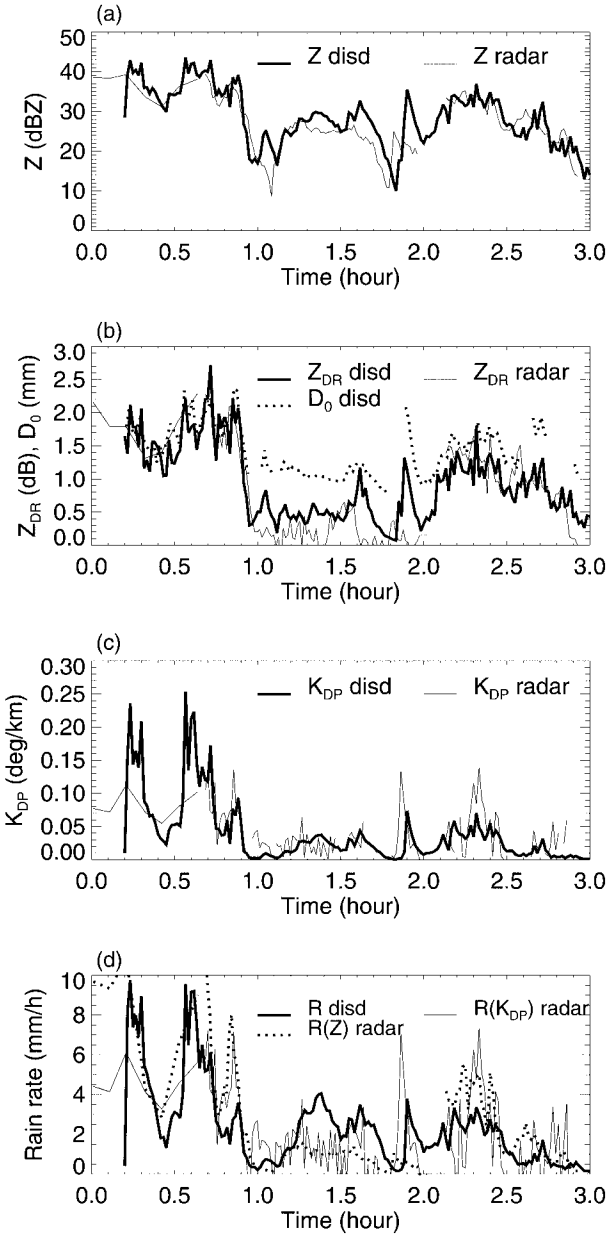

FIG. 4. Time series data of (a) disdrometer and CIM radar reflectivity (dBZ), (b) DSD median volume diameter (mm) and disdrometer and CIM radar Z_{DR} (dB), (c) disdrometer and CIM radar K_{DP} (° km^{-1}), and (d) disdrometer-, CIM radar Z-, and CIM radar K_{DP}-based rainfall rates (mm h^{-1}) for the weak convective rainband event.

this event were observed. By 1.0 h, the number of drops with D less than 1 mm had increased slightly and all drops had a D of less than 2 mm. This was associated with a dramatic ~2.0 dB decrease in both disdrometer and radar Z_{DR} (see Fig. 4b). A similar evolution can be seen between approximately 1.6 and 1.8 h. This kind of evolution may be a common feature for many precipitation events. That is, the DSD in the early stages of a convective cell is often dominated by an abundance of large drops with high fall speeds that are either the result of coalescence growth in the convective updraft (and fall to ground before significant drop breakup occurs) or originate as melting hail aloft (and fall to ground while still containing ice cores). In this particular case, we believe these drops were likely the result of a coalescence growth.

On this day, CIM experienced miscalibration problems that resulted in a substantial underestimation of Z. We therefore use the WSR-88D data to correct Z, with the corrected Z showing good agreement with that computed from the disdrometer data (Fig. 4a). The Z_{DR} measured by CIM also compares well with that from the disdrometer (Fig. 4b). The only exception is a noticeable discrepancy between 1.0 and 2.0 h. In this time period, a low signal-to-noise ratio resulting from the low rain rate and low uncorrected Z caused a negative bias in the radar Z_{DR}. The K_{DP} estimated by the radar does not differ much from the disdrometer estimate for light stratiform rain within the time interval between 1.0 and 3.0 h (Fig. 4c). This, however, is not the case for the small convective cells observed during the first hour of simultaneous data collection where the radar K_{DP} estimator tends to miss the peak values of K_{DP} retrieved from the disdrometer. Because the radar Zs are mostly less than 40 dBZ (even in the convective portions), the wide averaging window was used to obtain K_{DP} estimate. This type of averaging inevitably smears radial K_{DP} profiles, which can cause errors in pointwise K_{DP} estimates. Nevertheless, the smearing effect does not cause a bias in areal rainfall estimates, provided that dimensions of

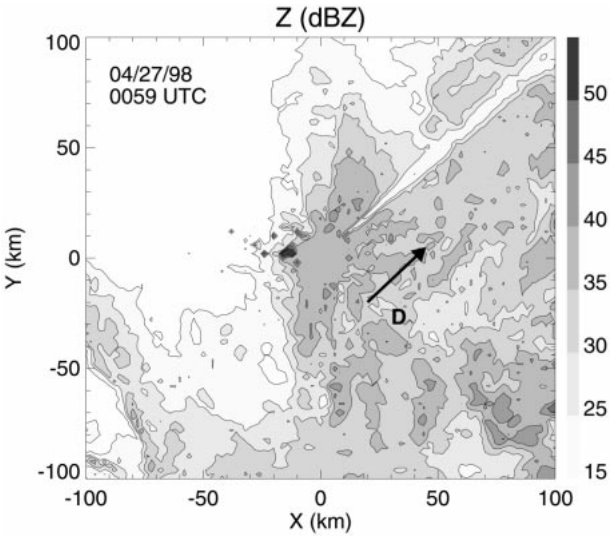

FIG. 5. Same as Fig. 2, but for the widespread stratiform precipitation event at 0059 UTC (3.5 h in Figs. 6 and 7).

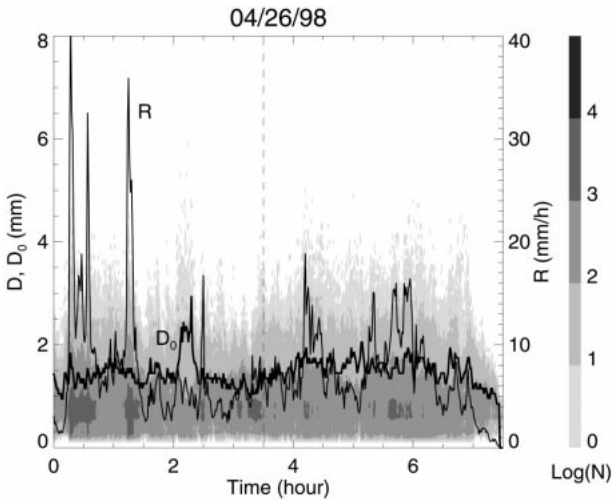

FIG. 6. Same as Fig. 3, but for the widespread stratiform precipitation event (26 Apr 1998). Dashed vertical line depicts time of the low-level reflectivity plot in Fig. 5.

the area exceed the width of the averaging window (Ryzhkov et al. 2000).

Because of the substantial difference in the disdrometer and radar update times (1 and 6 min, respectively), it is difficult to make comparisons of the rain rate derived from the disdrometer and the radar during the first 0.7 h of observations (Fig. 4d). Later, however, the radar scanning strategy was changed and the update rates became more compatible. In Fig. 4d we can identify two intervals (0.75–0.9 h and 2.2–2.4 h) in which both radar algorithms, $R(Z)$ and $R(K_{DP})$, overestimate the actual rain rate. On the other hand, the rain rate is underestimated by the radar from 1.2 to 1.8 h. These biases can be explained after examining the DSD and Z_{DR} evolution (Figs. 3 and 4b). In all three time intervals, rain rate varies in the same range (2–4 mm h^{-1}), whereas both DSD and Z_{DR} are different. The periods of underestimation (overestimation) are characterized by low (high) values of D_0 and Z_{DR} (during underestimation, all drops in the corresponding DSD are < 2 mm in diameter). A similar relation between rainfall underestimation (overestimation) and low (high) radar Z_{DR} was noted by Fulton et al. (1999).

b. Widespread stratiform precipitation

During 26–27 April 1998, a late spring storm system produced significant precipitation over central Oklahoma, with over 9 h of continuous precipitation recorded at the disdrometer site. Here we present data from a 7.5-h period during which both disdrometer and radar data were collected. The disdrometer recorded 55.7 mm of rain while the rain gauge at the Oklahoma Mesonet site recorded 57.1 mm of rainfall. This good agreement is likely due to the widespread and stratiform nature of the precipitation. Though strong convective cells with small hail occurred early (no hail was recorded at the disdrometer site), most of the rain was from widespread stratiform precipitation. The maximum rain rate recorded by the disdrometer was 41.68 mm h^{-1}. Figure 5 depicts CIM low-level radar reflectivity at 0059 UTC (3.5 h in Figs. 6 and 7). Storm motion was toward the NE. Overall, low-level radar reflectivities and disdrometer-measured rain rates were somewhat higher than those for the weak convective rainband case.

The DSD evolution for this event is shown in Fig. 6. It complements Fig. 7, which depicts a four-panel time series comparison of disdrometer and radar Z, Z_{DR}, K_{DP}, and rainfall rates. As in the previous case, occasional drops with D of greater than 5 mm were observed. Despite the relative stratiform nature of the precipitation throughout most of this event, significant variability existed in the drop spectrum. In particular, the two convective cells at approximately 0.25 and 1.25 h had a much larger than average number of drops at all sizes below 4.5 mm (but no drops with $D > 4.5$ mm). On the other hand, at 2.25 h, three drops with D greater than 5 mm were observed in a region where the precipitation intensity was much weaker. This feature was associated with approximately a 1.5-dB increase in Z_{DR} and a 10-dBZ increase in Z, but no appreciable increase in the rain rate (apparently a consequence of a few very large rain drops affecting Z_{DR} and Z much more than rain rate). It is interesting to note that the maximum D_0 for this event did not occur in a convective core, but rather in this relatively stratiform region of precipitation (at 2.25 h) where the rain rate was comparatively low, and the large drops were likely the product of melted large aggregates. Indeed, the D_0 at the time of maximum rain rate is almost a full millimeter smaller than the maximum D_0 recorded for this event. At 2.5 h, a sudden

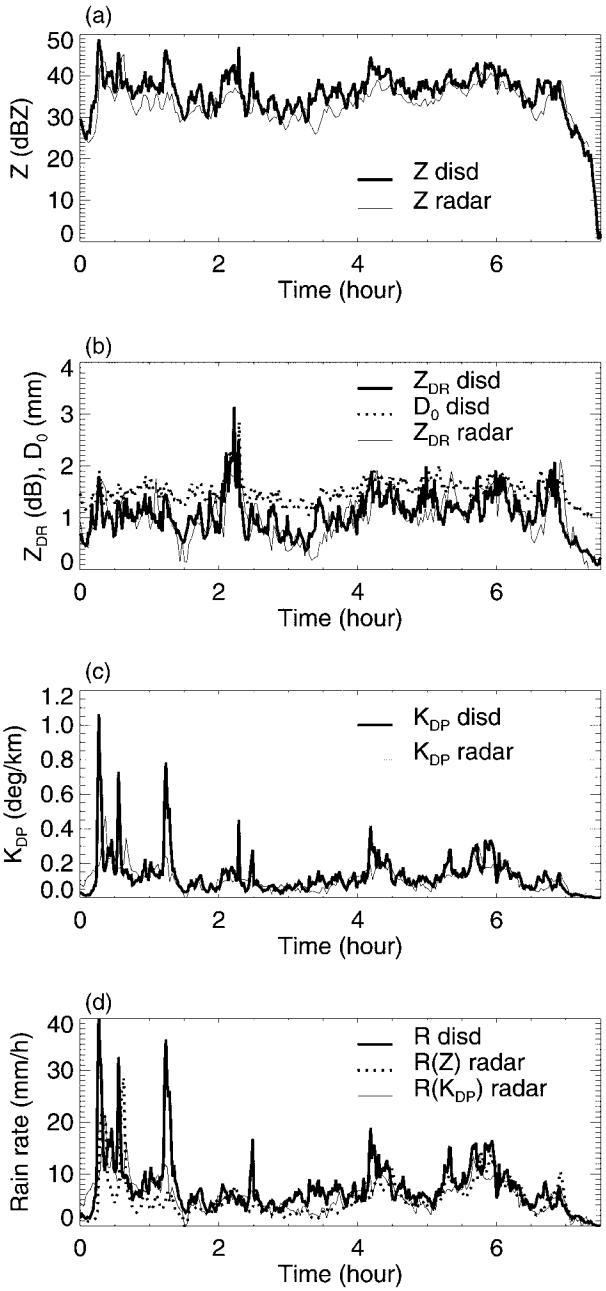

FIG. 7. Same as Fig. 4, but for the widespread stratiform precipitation event.

increase in the number of small drops caused a dramatic increase in precipitation rate but relatively small increases in both Z_{DR} and Z. Another interesting feature can be seen from 3.0 to 3.5 h. During this time period, the DSD was clearly dominated by a large number of drops with D less than 1 mm; when compared with Fig. 7d, it can be seen that both $R(Z)$ and $R(K_{DP})$ underestimate the disdrometer rainfall rate.

Figure 7 depicts a time series comparison of disdrometer and polarimetric radar variables. Radar reflectivity measured by the radar is slightly lower on average than the one estimated from the disdrometer. It is likely that a miscalibration error has not been totally eliminated by using the WSR-88D data. On the other hand, the Z_{DR} measured by the radar agrees well with the disdrometer estimate except for a short interval around 3.3 h where radar Z and K_{DP} both differ from the disdrometer values. As in the previous case, the radar K_{DP} again misses peak disdrometer K_{DP} values for small convective elements because of the smoothing effects of radial averaging. The agreement is much better outside rain-rate peaks. Rain rate estimated from K_{DP} is in accord with actual rain rate obtained from the disdrometer for R between 3 and 15 mm h^{-1}. Here, $R(K_{DP})$ underestimates rain rate in the narrow peaks with R greater than 15 mm h^{-1} for the reasons mentioned above. The $R(Z)$ estimator performs worse than the $R(K_{DP})$ algorithm in the regions where the radar Z is noticeably lower than the disdrometer Z (especially within the 0.7–1.4-h time interval).

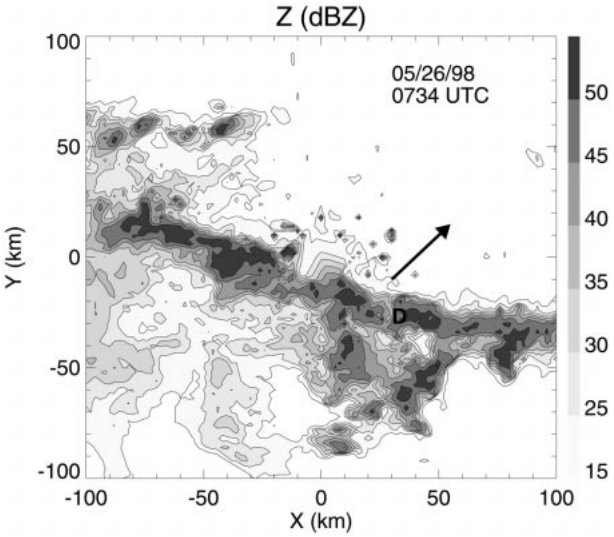

FIG. 8. Same as Fig. 2, but for the mesoscale convective system at 0734 UTC (21 min in Figs. 9 and 10).

c. Mesoscale convective system

On 26 May 1998, a leading-line/trailing-stratiform mesoscale convective system (MCS) passed through central Oklahoma. This MCS exhibited the precipitation features commonly attributed to this kind of convective system: an intense convective line followed by a weak reflectivity region known as a transition zone (Smull and Houze 1985) and a broad region of stratiform precipitation. In total, 13.6 mm of rain fell at the disdrometer site during this event, which compares well with the 11.2 mm measured at the Oklahoma Mesonet site. The maximum rain rate recorded by the disdrometer was 41.87 mm h^{-1}. Figure 8 depicts CIM low-level radar reflectivity at 0734 UTC (19 min in Figs. 9 and 10).

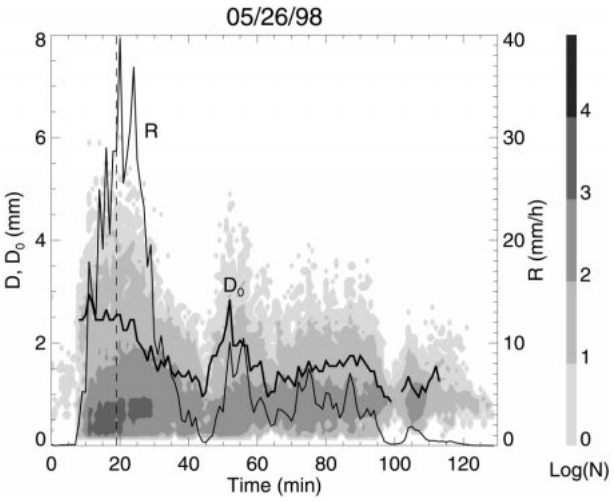

FIG. 9. Same as Fig. 3, but for the mesoscale convective system (26 May 1998). Dashed vertical line depicts time of the low-level reflectivity plot in Fig. 8.

Storm motion was toward the NE at ~16 m s^{-1}. The 2D video disdrometer documented the entire event; CIM radar data were first collected approximately 10 min after the leading edge of the convective line passed over the disdrometer site. WSR-88D data were not available for this case.

The DSD evolution for this event is shown in Fig. 9. It complements Fig. 10, which depicts a four-panel time series comparison of disdrometer and radar Z, Z_{DR}, K_{DP}, and rainfall rates. At the onset of the intense convective precipitation, a large number of raindrops occurred at all size categories. The largest raindrop recorded by the disdrometer during this convective event was 6.10 mm, and it occurred at the time of the maximum rainfall rate (a 8.46-mm particle was also recorded, but we believe that it was likely a hailstone). After the most intense portion of the convective line had passed, the concentrations at all sizes dropped off substantially and quickly reached a minimum in the transition zone region where the maximum drop size was a mere 2 mm. Within only a few minutes of this transition zone minimum, however, a surprising number of large drops fell in conjunction with the onset of stratiform precipitation. In fact, several drops with D greater than 4 mm fell within 5–10 min of the transition zone minimum. We believe that these large drops were likely the result of ice particles that were detrained from the upper portions of the convective line and bridged the transition zone region before melting.

As can be seen from Fig. 10, the maximum D_0 for this event occurred a few minutes before the onset of the heaviest precipitation in association with a DSD that contained many large drops (a feature that is also noted at the leading edge of the supercell thunderstorm case). On the other hand, the D_0 in the 5- to 10-min period after the transition zone minimum (at 52 min in Figs. 9 and 10, corresponding to a stratiform rain rate of only 10.08 mm h^{-1}) was only slightly smaller. Note that five drops with D greater than 5 mm were sampled over the 1-min period during which the maximum disdrometer rain rate occurred. Large drops, although significant contributors to most radar measurands, typically have very low number concentrations. Therefore, because of

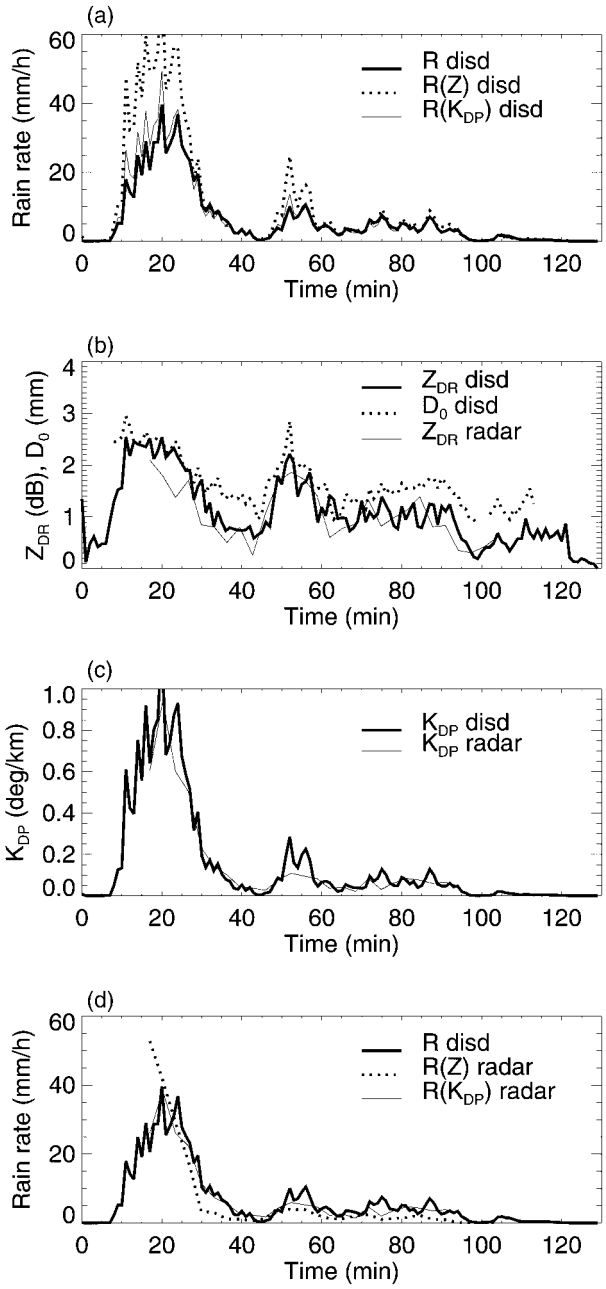

FIG. 10. Time series data of (a) actual, $R(Z)$, and $R(K_{DP})$ disdrometer rain rates (mm h^{-1}), (b) DSD median volume diameter (mm) and disdrometer and CIM radar Z_{DR} (dB), (c) disdrometer and CIM radar K_{DP} (° km^{-1}), and (d) disdrometer-, CIM radar Z-, and CIM radar K_{DP}-based rainfall rates (mm h^{-1}) for the mesoscale convective system.

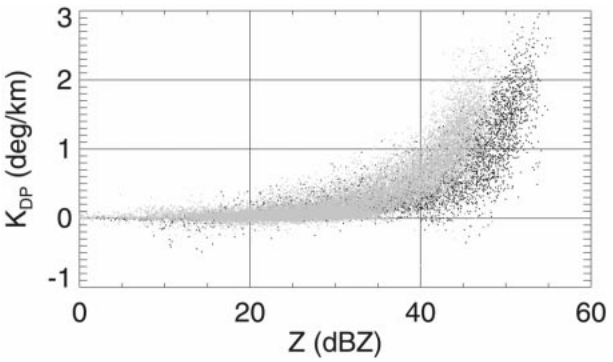

FIG. 11. Scattergram of CIM radar reflectivity (Z) and specific differential phase (K_{DP}) for the mesoscale convective system. Black dots correspond to the Z–K_{DP} pairs obtained for the first three scans when the leading edge of the squall line was in the middle of the examined area; gray dots correspond to the Z–K_{DP} pairs from the remaining 16 scans when the squall line was mostly at the periphery or outside the area of interest.

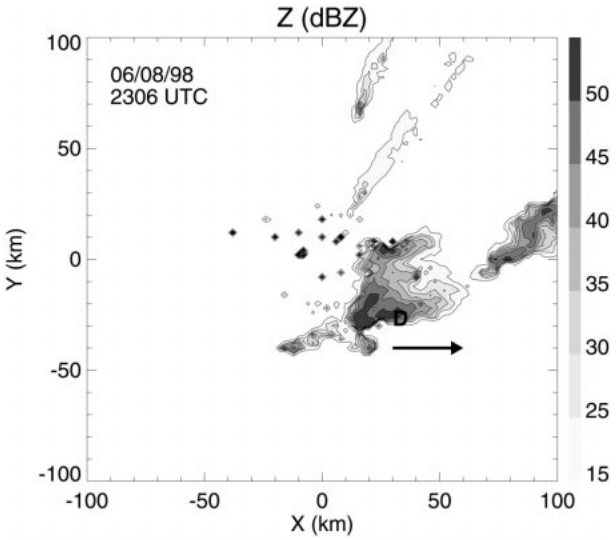

FIG. 12. Same as Fig. 2, but for the supercell thunderstorm at 2306 UTC (12 min in Figs. 12 and 13).

the small measurement area of the disdrometer, the likelihood of sampling a large drop for any given size bin is small. When a large drop is sampled, the calculated number concentration for that size bin is unrealistically high. This sampling problem results in zero concentrations for some drop sizes and unrealistically large concentrations at others, giving the DSD a ''spiked'' appearance, and makes comparisons between disdrometer and radar measurements very difficult. This problem is addressed in more detail in both section 5 and the appendix.

Time series of disdrometer rain rate, $R(Z)$, and $R(K_{DP})$ are displayed in Fig. 10a. Within the squall line and leading part of a stratiform region (immediately following the transition zone), the $R(Z)$ relation significantly overestimates actual rainfall because of the presence of the large drops. As expected, these regions are also characterized by high Z_{DR}. In contrast, because K_{DP} is less weighted by large drops than Z is, $R(K_{DP})$ estimates the actual rain rate almost perfectly. Here, K_{DP} and $R(K_{DP})$ estimated from the radar agree well with corresponding variables derived from the disdrometer. However, a noticeable discrepancy can be seen in the stratiform-region rain peak from 52 to 58 min. This discrepancy can be attributed to extra radial smoothing of K_{DP}, because measured Z is well below 40-dBZ threshold in that region.

It is interesting that the rain-rate estimate obtained from the radar using the standard WSR-88D $R(Z)$ algorithm is negatively biased everywhere except at the leading edge of the squall line (where it has a large positive bias, see Fig. 10d). Whereas a negative bias can be explained by radar miscalibration, a positive bias can be entirely attributed to the presence of large drops (with sizes in the 5- to 6-mm range according to Fig. 9). Additional evidence for this comes from the Z–K_{DP} scattergram presented in Fig. 11. This scattergram was obtained from analyzing Z–K_{DP} pairs within a 40 km × 40 km region centered on the disdrometer location. Data from 19 consecutive, 3-min scans at the elevation of 0.5° are presented. Black dots in Fig. 11 correspond to the Z–K_{DP} pairs obtained for the first three scans when the leading edge of squall line was right in the middle of the examined area; gray dots correspond to the Z–K_{DP} pairs from the remaining 16 scans when the squall line was mostly at the periphery or outside the area of interest. The scattergram shows different types of rain, one of which (corresponding to the black dots) is characterized by the DSD dominated by very large drops. This scattergram is shifted toward larger Zs by almost 5 dBZ. This fact underscores a need to use either different $R(Z)$ relations for different parts of an MCS or polarimetric algorithms that are more immune to DSD variations. In this case, the $R(K_{DP})$ relation is definitely superior to the $R(Z)$ algorithm but, as mentioned before, is also not totally immune to the DSD variability.

d. Supercell thunderstorm

We examine an intense supercell storm that occurred on 8 June 1998. Though the event was relatively short-lived, it produced rainfall rates as high as 81 mm h^{-1}, hail up to 2 cm in diameter, and winds greater than 30 m s^{-1}. Figure 12 depicts CIM low-level radar reflectivity at 2306 UTC (12 min in Figs. 13 and 14). Storm motion was toward the E at ~20 m s^{-1}. As can be seen from Fig. 12, the storm structure exhibited a classic ''hook'' shape that is characteristic of quasi-steady tornadic supercell thunderstorms. Though the storm was nontornadic at the time it passed over the disdrometer site (slightly north of the mesocyclone), it did produce a weak tornado ~1.5 h later. The disdrometer measured 9.5 mm of rainfall while the rain gauge at the Oklahoma Mesonet site measured 17.5 mm of total rain. We believe

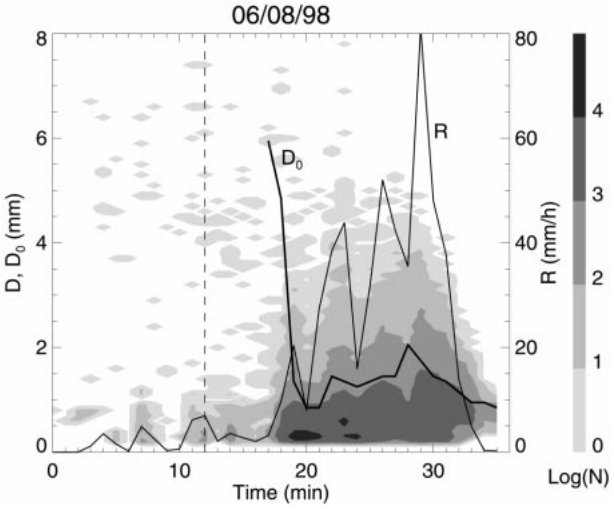

FIG. 13. Same as Fig. 3, but for the supercell thunderstorm (8 Jun 1998). Dashed vertical line depicts time of the low-level reflectivity plot in Fig. 12.

this discrepancy was likely due to two reasons. First, the highly compact, convective nature of this event meant that precipitation measurements separated by as little as 3 km could differ significantly. Second, however, we believe that high winds likely resulted in severe undercatchment by the disdrometer. We address this possibility in more detail in section 4.

The DSD evolution for this event is shown in Fig. 13. It complements Fig. 14, which depicts a time series comparison of disdrometer and radar rain rates, disdrometer-measured D_0, and radar Z_{DR}. Probably the most notable feature early on in this convective event is the approximate 15-min period that preceded the onset of intense precipitation, during which the DSD contained many big drops. In fact, a total of 54 drops with D greater than 5 mm were recorded during this event, many before the onset of heaviest precipitation. Once the intense precipitation began, the number of drops with D less than 1 mm increased dramatically, resulting in a DSD that had a much larger small drop concentration than was measured for any of the previous three cases. At 17 min, both the rain rate and concentrations for all drops with D less than 4 mm began a dramatic increase that, overall, would last for approximately 10 min. During this time, three distinct peaks in the disdrometer-measured rain rate are probably correlated with sudden increases in small drop concentrations (e.g., at 23, 26, and 29 min in Fig. 13). At 30 min, concentrations at all sizes decreased abruptly as the precipitation rate diminished and the storm moved past the disdrometer site.

Figure 14 depicts a time series comparison of disdrometer and polarimetric radar variables. Given the complicated spatial and temporal structure of this storm, good agreement between pointwise rainfall estimates obtained from the radar and disdrometer is not expected. Most interesting, perhaps, are the extremely large median volume diameters ($D_0 > 5$ mm) accompanied by very high differential reflectivities ($Z_{DR} > 3$ dB) that were observed at the leading edge of the storm. Both radar rainfall estimators, $R(Z)$ and $R(K_{DP})$, overestimate the rain rate during much of the storm. Overestimation by the $R(Z)$ algorithm is largest from 20 to 23 min when

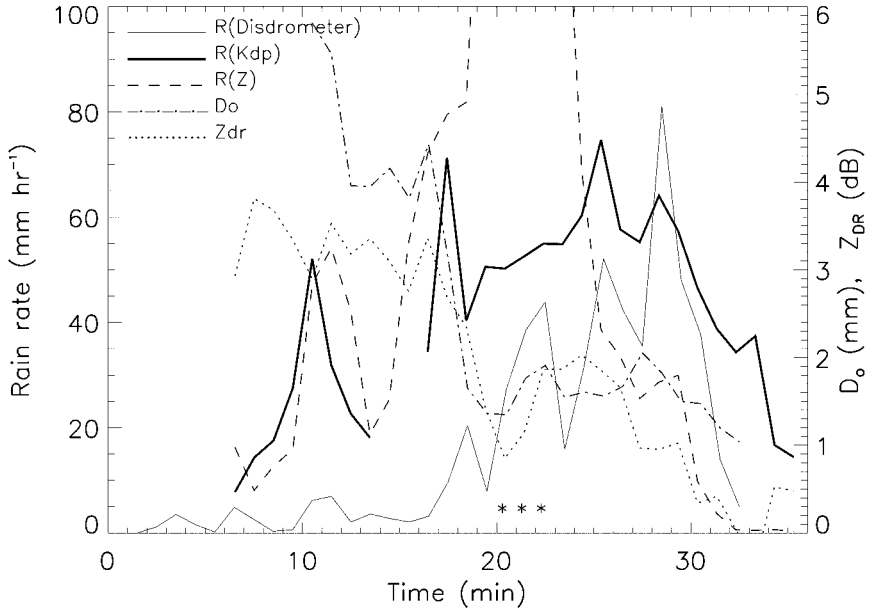

FIG. 14. Time series of DSD median volume diameter (mm), CIM radar Z_{DR} (dB), and disdrometer-, CIM radar Z-, and CIM radar K_{DP}-based rainfall rates (mm h^{-1}) for the supercell thunderstorm. Asterisks (*) indicate times the disdrometer recorded hailstones.

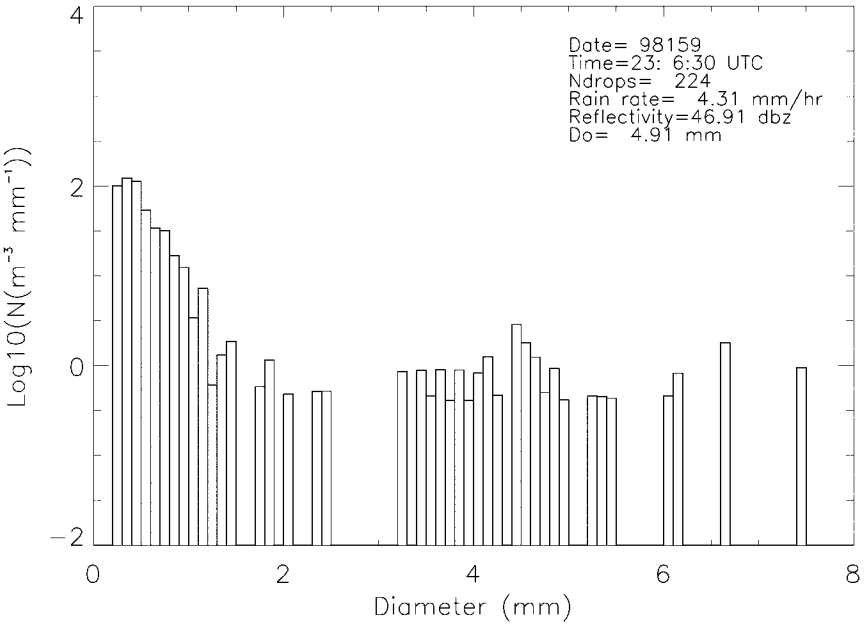

FIG. 15. Five-min-averaged DSD at the leading edge of the supercell thunderstorm case at 2306:30 UTC (12.5 min in Figs. 13 and 14).

the disdrometer recorded three hailstones (sizes up to 16 mm, indicated by the asterisks in Fig. 14). Differential reflectivity drops below 1 dB during this time interval, which is a clear indication of hail. It is obvious that the $R(K_{DP})$ estimator is much less prone to the presence of hail and exhibits only modest rainfall overestimation for the 20 to 23 min period. We can attribute this overestimation either to nonrandom orientation of hail and graupel or, possibly, to disdrometer undercatchment caused by the high winds (>30 m s^{-1}) associated with this storm. The $R(Z)$ and $R(K_{DP})$ estimates of rain rate are consistent during the initial phase of the storm (the 7- to 17-min time interval) but both greatly overestimate rain rate recorded by the disdrometer. This is likely caused by a very unusual type of DSD that is so different from the Marshall–Palmer or feasible gamma-type distributions from which existing polarimetric rainfall algorithms were initially derived.

An example of such a DSD is depicted in Fig. 15, which shows a 5-min average DSD at 12 min [a time when the distribution contained many large drops, similar to that presented by Beard et al. (1986) for a shallow convective cloud]. Applying the WSR-88D *Z–R* relationship [Eq. (5)] to the reflectivity computed from this DSD gives a rain rate of 38.14 mm h^{-1}, which is almost a factor of 9 times larger than the 4.31 mm h^{-1} indicated by the disdrometer. Given this unusual DSD, which contains many large drops, it is likely that rainfall estimation using K_{DP} is also biased. In an attempt to correct for this, Ryzhkov et al. (1999) developed a technique in which regions of large drops are first identified using polarimetric variables in a fuzzy logic routine. Knowledge of the predominant rain class is then used to adjust rain-rate estimates.

4. Functional fits

In this section, we examine and compare the results of theoretical gamma functional fits to the spectra of the four case studies. The maximum and minimum μ (unitless), Λ (mm^{-1}), N_0 (mm$^{-1-\mu}$ m^{-3}), N_0^* (m^{-4}), and D_0 (mm) parameters are presented in Table 1, and the event-average μ, Λ, N_0, and N_0^* parameters are presented in Table 2. The D_0s presented here are computed using parameters derived from the gamma functional fit [Eq. (2)] rather than directly from the counts of the disdro-

TABLE 1. Maximum and minimum of gamma functional fit parameters (calculated with minimum thresholds of 25 drops and 0.5 mm h^{-1}).

	μ		Λ		Log(N_0)		Log(N_0^*)		D_0	
	Min	Max	Min	Max	Min	Max	Min	Max	Min	Max
Case 1	−0.94	31.73	1.29	45.46	2.47	21.68	5.25	7.21	0.78	2.37
Case 2	−0.77	20.88	1.29	24.91	2.54	13.11	4.97	7.38	0.99	2.85
Case 3	−0.62	14.03	1.00	16.54	2.90	9.70	5.31	6.82	1.03	3.06
Case 4	−2.20	12.58	0.61	9.65	−2.37	7.20	4.01	7.60	1.04	5.82

TABLE 2. Averages of gamma functional fit parameters (calculated with minimum thresholds of 25 drops and 0.5 mm h^{-1}).

	μ	Λ	Log(N_0)	Log(N_0^*)
Case 1	3.99	6.39	4.97	6.32
Case 2	2.89	4.59	4.56	6.59
Case 3	2.79	4.20	4.18	6.33
Case 4	2.89	2.83	2.88	6.19

TABLE 3. Comparison of maximum gamma functional fit parameters for minimum rain-rate thresholds of 0.5 and 1.0 mm h^{-1}.

	μ		Λ		Log(N_0)	
	0.5	1.0	0.5	1.0	0.5	1.0
Case 1	31.73	29.60	45.46	36.73	21.68	18.59
Case 2	20.88	13.76	24.91	15.35	13.11	9.12
Case 3	14.03	14.03	16.54	16.54	9.70	9.70
Case 4	12.58	12.58	9.65	9.65	7.20	7.20

meter [Eq. (3)]. This is done 1) to demonstrate the differences in D_0 magnitudes resulting from these two methods (e.g., those plotted in Figs. 3, 6, 9, and 13) and 2) so that the results can be compared more easily to those of other studies (e.g., Tokay and Short 1996).

A detailed comparison of D_0 time series from these two methods (not shown) indicates that relative maximums and minimums in D_0 occurred at approximately the same times and locations in all four events. Furthermore, the D_0 magnitudes were generally in close agreement. Agreement in magnitude became poor, however, when clearly nongamma-type distributions were encountered (such as the large drop distributions near the leading edge of both the MCS and supercell storms). In general, maximum and average values for μ, Λ, and log(N_0) (see Tables 1 and 2) were smaller than those presented by Tokay and Short (1996). Note, however, that the maximum μ, Λ, and N_0 were found to be associated with the smallest rainfall rates for most cases. Therefore, the maximum and average parameter values probably are significantly influenced by the choice of the minimum rain-rate threshold. To ensure a sufficient number of drops for a meaningful functional fit, we chose those minimum thresholds to be 25 drops and 0.5 mm h^{-1} for this study. Tokay and Short (1996) used 10 drops and 0.1 mm h^{-1}, respectively.

To examine better this influence, we conducted an additional test wherein we computed parameters using thresholds of 25 drops and 1.0 mm h^{-1}. A comparison of how the maximum and average μ, Λ, and N_0 parameters change when the minimum rain-rate threshold is changed from 0.5 to 1.0 mm h^{-1} is presented in Tables 3 and 4, respectively. The tables clearly show that maximum and average μ, Λ, and N_0 parameters decreased when the higher rain-rate threshold was used, especially for events that contain periods of weak stratiform precipitation. This sensitivity to the method by which DSDs are determined should be kept in mind when comparing maximum and average gamma parameters from various studies, all of which may have different criteria for computing and evaluating DSDs.

5. Measurement errors

a. Drop shape distortions

As noted in section 2, the 2D video disdrometer is designed to obtain high-resolution measurements of drop shape. In quiescent wind conditions, accurate drop shapes are, in fact, measured. However, for the high wind speeds associated with many of the events in this study (and for Oklahoma precipitation events in general), our observations suggest that a combination of wind shear near ground level and airflow around the disdrometer results in disturbances that can occasionally distort the shapes of drops. A similar distortion of drop shape due to airflow disturbances has been noted in aircraft measurements (e.g., Beard et al. 1999) of drop shapes.

In an attempt to alleviate this problem, our future plans include installing the disdrometer in a pit. It is important to note that, although the drop shape is apparently affected by airflow disturbances, the drop size is not. As a result, we believe the DSDs presented in this paper are accurate. Indeed, this belief is strengthened by most of our disdrometer and radar K_{DP} and Z_{DR} comparisons. Recall from section 2 that we used an empirical drop shape formula derived by Beard and Chuang (1987) for the computation of our polarimetric measurements. With the possible exception of the supercell thunderstorm case for which we believe there was severe undercatchment, the overall agreement between disdrometer and radar K_{DP} and Z_{DR} is good. This result is an indirect indication that actual drop shapes do not differ much from the theoretical dependence given in Eq. (4).

b. Undercatchment in high winds

Another apparent artifact of ground-level wind shear and airflow disturbances around the disdrometer is an occasional undercatchment of drops. Using a numerical model, Nešpor et al. (2000) examined 2D video disdrometer drop trajectories for a variety of drop sizes, wind speeds, and wind directions. Depending on the wind direction and speed, they found that disdrometer

TABLE 4. Comparison of average gamma functional fit parameters for minimum rain-rate thresholds of 0.5 and 1.0 mm h^{-1}.

	μ		Λ		Log(N_0)	
	0.5	1.0	0.5	1.0	0.5	1.0
Case 1	3.99	3.51	6.39	5.83	4.97	4.81
Case 2	2.89	2.66	4.59	4.34	4.56	4.46
Case 3	2.79	2.79	4.20	4.20	4.18	4.18
Case 4	2.89	2.52	2.83	2.63	2.88	2.87

catchment errors were sometimes severe at the smaller drop sizes (though larger drops, with much higher fall speeds, were largely unaffected by the airflow). The results presented in Figs. 3, 6, 9, and 13 indicate that the periods of heaviest rainfall are typically associated with DSDs that are characterized by an abundance of small drops.

In our study, we often encountered wind speeds that were much higher than those modeled by Nešpor et al. (2000) and occasionally noted instances where there appeared to be severe undercatchment at many drop sizes (though comparisons of rainfall totals with that from a rain gauge located 3 km from the disdrometer were in close agreement for all but the highest wind cases). To test this further, we filtered the data to examine and compare the DSDs measured by each 5 cm $\times$ 5 cm quadrant of the measurement area. Those observations (not shown) indicate that there were indeed cases in which there were discrepancies in both the number of drops and DSDs measured within each quadrant of the measurement area (particularly for the supercell thunderstorm, for which maximum wind speeds were >30 m s^{-1}). This result demonstrates that DSDs measured by the 2D video disdrometer should be viewed with caution when examining data collected during high wind events. As with the drop distortions noted earlier, we hope to mitigate this problem by eventually installing the disdrometer in a pit.

c. *Limited spatial resolution of disdrometer measurements*

We note the difficulties that arise when attempting to compare data from the vastly different disdrometer and radar sampling volumes. As noted earlier, this problem is particularly acute for large drop sizes which, although significant contributors to most radar measurands, typically have very low number concentrations. Therefore, at most times, large drops within a specific size category are not sampled by the disdrometer (even though their actual concentration is nonzero). On the other hand, if even a single large drop is sampled, the assumed number of drops (mm^{-3} mm^{-1}) in that size category is then computed using the formula

$$N(D_i) = \frac{1}{\Delta T \Delta D} \sum_{j=1} \frac{1}{A_j v_j}, \tag{7}$$

where D_i is the diameter of category i, ΔT is the integration time (60 s), ΔD is the width of the size class (0.1 mm), A_j is the disdrometer effective measurement area (see section 2) during the collection of drop j, and v_j is the fall speed of drop j. More often than not, this will result in an estimated number concentration for that particular drop size that is unrealistically high (indicated by a spike in the DSD). To quantify these sampling volume discrepancies, especially for the larger drop sizes, we statistically address the accuracy of disdrometer R, $Z_{h,v}$, Z_{DR}, and K_{DP} measurements in the appendix.

6. Discussion and conclusions

We have examined DSDs from four, very different precipitation events: weak convective rainbands, widespread stratiform precipitation, a mesoscale convective system, and a supercell thunderstorm. Our observations indicate that significant DSD variability exists not only from one event to the next, but also within individual precipitation events. Despite their greatly different origins, rain rates, and storm structures, we also found that large raindrops with diameters greater than 5 mm were common to each system.

The data indicate that the maximum D_0 is not always associated with the heaviest rainfall but is sometimes found either in advance of convective cores or, occasionally, in stratiform regions where the rain rates are relatively low. For cases where the maximum D_0 occurs in the convective line, they can be attributed to an abundance of large drops with high fall speeds that either originate as melting hail aloft (and fall to ground while still containing ice cores) or are the result of coalescence growth in the convective updraft (and fall to ground before significant drop breakup occurs). In the case where the maximum D_0 occurs in stratiform precipitation, we believe the large raindrops are primarily the result of the melting of large aggregates.

Overall agreement of disdrometer and polarimetric radar measurements of Z, Z_{DR}, K_{DP}, $R(Z)$, and $R(K_{DP})$ is good. However, there are situations in which agreement is poor. For example, during periods of radar $R(Z)$ and $R(K_{DP})$ underestimation, the DSD is typically characterized by an abundance of small drops (and small D_0); during periods of radar $R(Z)$ and $R(K_{DP})$ overestimation, the DSD is typically characterized by an abundance of large drops (and large D_0). In particular, we observe ''plateaulike'' DSDs that contain a large number of very big ($D > 6$ mm) drops near the leading edge of intense convective cells. These DSDs are also characterized by very large disdrometer and radar Z and Z_{DR}. Because of their unusual structure, these DSDs are poorly represented by gamma function fits and, subsequently, by many polarimetric rainfall algorithms (many of which have been derived using assumed ranges of gamma μ, Λ, and N_0 parameters). These observations indicate that an a priori classification of different rain types associated with different DSDs should be an essential part of polarimetric rainfall estimation. Additionally, good agreement between Z_{DR} obtained from disdrometer and dual-polarization radar as well as high correlation between D_0 and Z_{DR} confirms that Z_{DR} is a key parameter to distinguish between different types of rain and associated DSDs. Thus, using Z_{DR} jointly with either Z or K_{DP} provides the basis for further improvement of radar rainfall estimation.

Overall, the maximum and average of gamma μ, Λ, and N_0 parameters are slightly smaller than those presented by Tokay and Short (1996). We note, however, that the maximum and average values are dependent on

the thresholds used to define a DSD. That is, to ensure a sufficient number of drops for a meaningful functional fit, we chose a minimum, 1-min rain-rate threshold of 0.5 mm h^{-1}. If this threshold is simply changed from 0.5 to 1.0 mm h^{-1}, the maximum and average μ, Λ, and N_0 values decrease (quite dramatically for the precipitation events that are dominated by low rain rates). This sensitivity to the method by which DSDs are determined should be kept in mind when comparing maximum and average gamma parameters from various studies, all of which may have different criteria for computing and evaluating DSDs.

Our experience with 2D video disdrometer measurements indicates that ground-level shear and airflow disturbances around the disdrometer occasionally cause disturbances that distort drop shapes. For very high wind events, there are also indications that severe undercatchment might occur. We hope to mitigate both of these problems in the future by installing the disdrometer in a pit or, possibly, on a tower. Owing to their significantly different sampling volumes, we also conclude that comparisons between disdrometer and radar measurements are occasionally difficult. Despite these uncertainties, we believe the new 2D video disdrometer offers an opportunity to measure DSDs with unprecedented accuracy.

Acknowledgments. We thank the many NSSL scientists, technicians, and computer support personnel who provided assistance with the shipping and installation of the 2D video disdrometer. In particular, Sherman Fredrickson has been instrumental in providing general maintenance and calibration expertise. Mike Schmidt and Richard Wahkinney have maintained and calibrated the Cimarron radar. The comments of Richard Fulton and two anonymous reviewers are also greatly appreciated. The leasing of the Joanneum Research 2D video disdrometer during the 1998 spring season was supported by the NSSL Director's Discretionary Fund. This work was partially supported by the NSF Grant ATM-9907930.

APPENDIX

An Accuracy of the R, $Z_{h,v}$, Z_{DR}, and K_{DP} Estimates from Disdrometer Data

Rainfall rate, radar reflectivity factors at horizontal and vertical polarizations $Z_{h,v}$, and specific differential phase K_{DP} can be estimated from the disdrometer data using the following formulas

$$R\ (\text{mm h}^{-1}) = \sum_i r_i \frac{N_i}{V_i},$$

$$Z_{h,v}\ (\text{mm}^6\ \text{m}^{-3}) = \sum_i z_{h,v}^{(i)} \frac{N_i}{V_i}, \quad \text{and}$$

$$K_{DP}\ (^\circ\ \text{km}^{-1}) = \sum_i k_{dp}^{(i)} \frac{N_i}{V_i}, \tag{A1}$$

where i designates the ith interval of drop diameters, N_i is a number of drops caught by the disdrometer within this interval of sizes,

$$r_i = 0.6 \times 10^{-3} \pi w_t^{(i)} D_i^3,$$

$$z_{h,v}^{(i)} = \frac{4\lambda^4 |f_{h,v}^{(i)}|^2}{\pi^4 |(\varepsilon - 1)/(\varepsilon + 2)|^2},$$

$$k_{dp}^{(i)} = \frac{0.18\lambda}{\pi} \text{Re}[f_h^{(i)} - f_v^{(i)}], \quad \text{and} \quad V_i = w_t^{(i)} AT, \tag{A2}$$

and D_i (mm) is an equivolume diameter of a drop, $w_t^{(i)}$ (m s^{-1}) is a terminal velocity of a drop with diameter D_i, λ (mm) is a radar wavelength, $f_{h,v}^{(i)}$ (mm) is a complex scattering amplitude of the drop with diameter D_i at horizontal or vertical polarization, ε is a dielectric constant of water, V_i (m^3) is a sampling volume for the drops in the ith size category, A (m^2) is an exposure area of the disdrometer (0.0081 m^2 in our case), and T (s) is an accumulation time (typically 60 s).

Because N_i is a random number, the variables R, Z_h, Z_v (or $Z_{DR} = Z_h/Z_v$), and K_{DP} are also random. It is well known that N_i is distributed according to Poisson law (Joss and Waldvogel 1969; Smith et al. 1993):

$$p(N_i) = \frac{(\overline{N_i})}{N_i!} e^{-\overline{N_i}}, \tag{A3}$$

where $\overline{N_i}$ is the average number of drops in the ith category of sizes. Therefore, the contribution X_i of the drops in the ith size category to the variables R, Z_h, Z_v, and K_{DP} ($X_i = r_i N_i/V_i$, for example) also has Poisson distribution. Fractional standard deviation of this distribution determined as $[\text{var}(X_i)]^{1/2}/\overline{X_i}$ is equal to $[\text{var}(N_i)]^{1/2}/\overline{N_i} = (\overline{N_i})^{-1/2}$ for the Poisson law. The average number of drops $\overline{N_i}$ decreases rapidly with increasing diameter and can be much smaller than 1 for very large drop sizes. This implies that the 2D video disdrometer will, most of the time, record no drops in the interval centered at fairly large drop diameter (say, over 5 mm) and $\overline{N_i} \ll 1$. As a result, the fractional standard deviation $[\text{var}(X_i)]^{1/2}/\overline{X_i}$ for large drops can be very high. In other words, larger errors of the R, Z_h, Z_{DR}, and K_{DP} estimates from disdrometer data have to be expected if (a) total concentration of particles is small (this leads to decrease of $\overline{N_i}$ in all size bins), or (b) larger drops are in excess and small drops are in deficit. The latter augments relative weight of large drops.

The variance of the rain-rate R estimate from disdrometer can be expressed as

$$\text{var}(R) = \langle (R - \overline{R})^2 \rangle = \sum_i \left(\frac{r_i}{V_i} \right)^2 \langle (N_i - \overline{N_i})^2 \rangle$$

$$= \sum_i \left(\frac{r_i}{V_i} \right)^2 \overline{N_i}. \tag{A4}$$

After approximating the sum in Eq. (A4) by an integral, we obtain

$$\mathrm{var}(R) = \int \frac{r^2(D)}{V(D)} n(D)\, dD, \tag{A5}$$

where $n(D) = N(D)/V(D)$ is a drop concentration. The mean value of rain rate can be written as

$$\overline{R} = \int r(D) n(D)\, dD, \tag{A6}$$

and the fractional standard deviation of the R estimate from disdrometer FSD(R) is given by the formulas

$$\mathrm{FSD}(R) = \frac{\left[\int \frac{r^2(D)}{V(D)} n(D)\, dD\right]^{1/2}}{\int r(D) n(D)\, dD} = (AT)^{-1/2} \frac{\left[\int w_t(D) D^6 n(D)\, dD\right]^{1/2}}{\int w_t(D) D^3 n(D)\, dD}. \tag{A7}$$

From Eq. (A7) it is clear that FSD(R) is inversely proportional to the square root of the disdrometer sampling volume $w_t AT$. Similar formulas can be obtained for FSD($Z_{h,v}$) and FSD(K_{DP}):

$$\mathrm{FSD}(Z_{h,v}) = (AT)^{-1/2} \frac{\left[\int z^2_{h,v}(D) w_t^{-1}(D) n(D)\, dD\right]^{1/2}}{\int z_{h,v}(D) n(D)\, dD}, \tag{A8}$$

and

$$\mathrm{FSD}(K_{\mathrm{DP}}) = (AT)^{-1/2} \frac{\left[\int k_{\mathrm{dp}}(D) w_t^{-1}(D) n(D)\, dD\right]^{1/2}}{\int k_{\mathrm{dp}}(D) n(D)\, dD}. \tag{A9}$$

The expression for the fractional standard deviation of Z_{DR} is more complicated:

$$\mathrm{FSD}(Z_{\mathrm{DR}}) = [\mathrm{FSD}^2(Z_h) + \mathrm{FSD}^2(Z_v) - 2\,\mathrm{cov}_n(Z_h, Z_v)]^{1/2}, \tag{A10}$$

where the normalized covariance $\mathrm{cov}_n(Z_h, Z_v)$ is defined as

$$\mathrm{cov}_n = \frac{\int z_h(D) z_v(D) w_t^{-1}(D) n(D)\, dD}{AT \int z_h(D) n(D)\, dD \int z_v(D) n(D)\, dD}. \tag{A11}$$

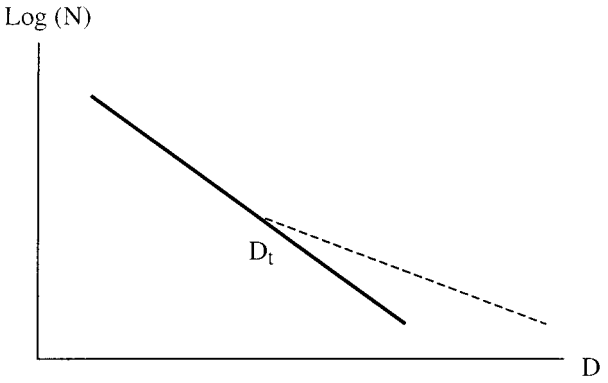

FIG. A1. Models of the exponential (solid line) and biexponential (dashed lined) DSDs.

We calculate FSD(R), FSD(Z_h), FSD(Z_{DR}), and FSD(K_{DP}) for two types of drop size distributions $n(D)$. The first one is the standard exponential Marshall–Palmer distribution $n(D) = N_0 e^{-\Lambda D}$, where $N_0 = 8000\ \mathrm{m}^{-3}\ \mathrm{mm}^{-1}$, $\Lambda\ (\mathrm{mm}^{-1}) = 4.1 R^{-0.21}$ (rain rate R is expressed in millimeters per hour), and the second one is a biexponential DSD that coincides with the Marshall–Palmer for drop sizes below D_t and has smaller slope Λ_t for D greater than D_t (see Fig. A1). Using biexponential DSD, we try to model the drop spectrum with an excess of large drops originating from melting hail and possibly containing ice cores inside. The results of computations according to Eqs. (A7)–(A10) are presented in Table A1 for different rain rates. We assumed that terminal velocity of raindrops is given by the formula

$$w_t = 3.78 D^{0.67}; \tag{A12}$$

drop shape changes with size according to the Eq. (3) recommended by Beard and Chuang (1987).

All computations were made for the wavelength of the Cimarron radar (10.97 cm) and integration in Eqs. (A7)–(A10) was performed in the range of equivolume diameters from 0 to 8 mm. We assumed also that, for biexponential DSD, $D_t = 5$ mm and $\Lambda_t = 1/2\Lambda$. All estimates were done for a disdrometer sampling time of 1 min.

It can be seen from Table A1 that the errors in estimating R and K_{DP} from the 2D video disdrometer 1-min samples are reasonably small and do not exceed 8% in the worst case. The standard errors of Z_h and Z_{DR} are more serious and vary between 0.7 and 3.1 dB for the radar reflectivity factor and 0.3 and 1.4 dB for differential reflectivity. The errors are generally smaller for higher rain rates, because the total number of drops is higher for more intense rainfall. In all cases, biexponential DSD gives larger errors in all estimated parameters. This increase is especially pronounced for Z_h and Z_{DR} because these variables are heavily weighted by large drops.

The calculations made so far were based on the assumption that drop counts N_i in each size interval are

TABLE A1. Fractional standard errors (FSD) of R, Z_h, Z_{DR}, and K_{DP}.

	Marshall–Palmer DSD rain rate (mm h^{-1})				Biexponential DSD rain rate (mm h^{-1})			
Variable	3	10	30	100	3	10	30	100
FSD(R)	0.076	0.062	0.051	0.040	0.077	0.065	0.058	0.048
FSD(Z_h)	0.328	0.277	0.221	0.147	0.475	0.516	0.365	0.178
FSD(Z_{DR})	0.104	0.111	0.096	0.061	0.241	0.282	0.174	0.066
FSD(K_{DP})	0.084	0.052	0.043	0.034	0.067	0.064	0.061	0.046

distributed according to the Poisson law. As was pointed out by Kostinski and Jameson (1997), a mixed Poissonian distribution is more appropriate to characterize the statistics of N_i. The variance of such distribution is generally larger than the one for ideal Poisson distribution. Therefore, the numbers in Table A1, in fact, characterize lower limit of actual fractional standard errors.

REFERENCES

Atlas, D., C. W. Ulbrich, F. D. Marks Jr., E. Amitai, and C. R. Williams, 1999: Systematic variation of drop size and radar-rainfall relations. *J. Geophys. Res.,* **104,** 6155–6169.

Battan, L. J., 1973: *Radar Observations of the Atmosphere.* University of Chicago Press, 324 pp.

Beard, K. V., and C. Chuang, 1987: A new model for the equilibrium shape of raindrops. *J. Atmos. Sci.,* **44,** 1509–1524.

——, D. B. Johnson, and D. Baumgardner, 1986: Aircraft observations of large raindrops in warm, shallow, convective clouds. *Geophys. Res. Lett.,* **13,** 991–994.

——, P. X. Xu, H. T. Ochs, and J. S. Naul, 1999: Raindrop axis ratios from aircraft 2DP measurements in CAPE for application to dual-polarization radar measurements. Preprints, *29th Conf. on Radar Meteorology,* Montreal, Canada, Amer. Meteor. Soc., 297–300.

Chandrasekar, V., V. N. Bringi., N. Balakrishnan, and D. S. Zrnić, 1990: Error structure of multiparameter radar and surface measurements of hail. Part III: Specific differential phase. *J. Atmos. Oceanic Technol.,* **7,** 621–629.

Dou, X., J. Testud, P. Amayenc, and R. Black, 1999: The concept of normalized gamma distribution to describe raindrop spectra, and its use to parameterize rain relations. Preprints, *29th Int. Conf. on Radar Meteorology,* Montreal, PQ, Canada, Amer. Meteor. Soc., 625–628.

Fulton, R. A., A. V. Ryzhkov, and D. S. Zrnić, 1999: Areal rainfall estimation using conventional and polarimetric radar methods. Preprints, *29th Int. Conf. on Radar Meteorology,* Montreal, PQ, Canada, Amer. Meteor. Soc., 293–296.

Joss, J., and A. Waldvogel, 1967: A raindrop spectrograph with automatic analysis. *Pure Appl. Geophys.,* **68,** 240–246.

——, and ——, 1969: Raindrop size distribution and sampling size errors. *J. Amos. Sci.,* **26,** 566–569.

Knollenberg, R. G., 1970: The optical array: An alternative to scattering or extinction for airborne particle size determination. *J. Appl. Meteor.,* **9,** 86–103.

Kostinski, A. B., and A. R. Jameson, 1997: Fluctuating properties of precipitation. Part I: On deviations of single-size drop counts from the Poisson distribution. *J. Atmos. Sci.,* **54,** 2174–2186.

Nešpor, V., W. Krajewski, and A. Kruger, 2000: Wind-induced error of rain drop size distribution using a two-dimensional video disdrometer. *J. Atmos. Oceanic Technol.,* **17,** 1483–1492.

Rowland, J. R., 1976: Comparison of two different raindrop disdrometers. Preprints, *17th Conf. on Radar Meteorology,* Seattle, WA, Amer. Meteor. Soc., 398–405.

Ryzhkov, A., and D. S. Zrnić, 1995: Comparison of dual-polarization radar estimators of rain. *J. Atmos. Oceanic Technol.,* **12,** 249–256.

——, and ——, 1996: Assessment of rainfall measurement that uses specific differential phase. *J. Appl. Meteor.,* **35,** 2080–2090.

——, R. Lopez, R. Fulton, D. Zrnić, T. Schuur, and Y. Liu, 1999: Hydrometeor classification with polarimetric radar for improved rainfall measurements and detection of hail and electrically charged regions. Preprints, *29th Int. Conf. on Radar Meteorology,* Montreal, PQ, Canada, Amer. Meteor. Soc., 289–292.

——, D. S. Zrnić, and R. A. Fulton, 2000: Areal rainfall estimates using differential phase. *J. Appl. Meteor.,* **39,** 263–268.

Scarchilli, G., E. Gorgucci, V. Chandrasekar, and T. A. Seliga, 1993: Rainfall estimation using polarimetric techniques at C-band frequencies. *J. Appl. Meteor.,* **32,** 1150–1160.

Schönhuber, M., H. E. Urban, P. P. V. Poiares Baptista, W. L. Randeu, and W. Riedler, 1997: Weather radar versus 2D-video-disdrometer data. *Weather Radar Technology for Water Resources Management,* B. Bragg Jr. and O. Massambani, Eds., Unesco Press, 159–171.

Schuur, T. J., A. V. Ryzhkov, D. S. Zrnić, and M. Schönhuber, 1999: Drop size distributions measured by a 2D-video-disdrometer. Comparison with dual-polarization radar data. Preprints, *29th Int. Conf. on Radar Meteorology,* Montreal, PQ, Canada, Amer. Meteor. Soc., 655–658.

Seliga, T. A., K. Aydin, and H. Direskeneli, 1986: Disdrometer measurements during an intense rainfall event in central Illinois: Implications for differential reflectivity radar observations. *J. Climate Appl. Meteor.,* **25,** 69–76.

Smith, P. L., Z. Liu, and J. Joss, 1993: A study of sampling-variability effects in raindrop size observations. *J. Appl. Meteor.,* **32,** 1259–1269.

Smull, B. F., and R. A. Houze Jr., 1985: A midlatitude squall line with a trailing region of stratiform rain: Radar and satellite observations. *Mon. Wea. Rev.,* **113,** 117–133.

Testud, J., E. Le Bouar, E. Obligis, and M. Ali-Mehenni, 2000: The rain profiling algorithm applied to polarimetric weather radar. *J. Atmos. Oceanic Technol.,* **17,** 332–356.

Tokay, A., and D. A. Short, 1996: Evidence from tropical raindrop spectra of the origin of rain from stratiform versus convective clouds. *J. Appl. Meteor.,* **35,** 355–371.

——, O. W. Thiele, A. Kruger, and W. F. Krajewski, 1999: New Measurements of drop size distribution and its impact on radar rainfall retrievals. Preprints, *29th Int. Conf. on Radar Meteorology,* Montreal, PQ, Canada, Amer. Meteor. Soc., 659–662.

Ulbrich, C. W., 1983: Natural variations in the analytical form of the raindrop size distribution. *J. Climate Appl. Meteor.,* **22,** 1764–1775.

——, 1985: The effects of drop size distribution truncation on rainfall integral parameters and empirical relations. *J. Climate Appl. Meteor.,* **24,** 580–590.

——, and D. Atlas, 1998: Rainfall microphysics and radar properties: Analysis methods for drop size spectra. *J. Appl. Meteor.,* **37,** 912–923.

Waldvogel, A., 1974: The N_0 jump of the raindrop spectra. *J. Atmos. Sci.,* **31,** 1067–1078.

Williams, C. R., P. E. Johnston, W. L. Ecklund, K. S. Gage, and D. A. Carter, 2000: Rain drop size distribution deduced from UHF and S-band profilers used in support of ground validation of the TRMM satellite. *Proc. URSI National Radio Science Meeting,* Boulder, CO, International Union of Radio Science, 296.